



Synergistic enhancement of solar H₂O₂ and HCOOH production over TiO₂ by dual co-catalyst loading in a tri-phase system

Bowen He^a, Cheng Luo^a, Zhongliao Wang^a, Liuyang Zhang^{b,*}, Jiaguo Yu^{a,b,**}

^a State Key Laboratory of Advanced Technology for Materials Synthesis and Processing, International School of Material Science and Engineering, Wuhan University of Technology, Wuhan 430070, PR China

^b Laboratory of Solar Fuel, Faculty of Materials Science and Chemistry, China University of Geosciences, 388 Lumo Road, Wuhan 430074, PR China

ARTICLE INFO

Keywords:

Dual cocatalysts
Photocatalytic hydrogen peroxide
Formic acid
Triphase system
Electronic distribution modulation

ABSTRACT

Cocatalysts, especially precious metallic cocatalysts, are predominant in promoting photocatalytic H₂O₂ production. However, chemisorbed H₂O₂ is exceedingly apt to decompose on newly formed Pt(O). Herein, the dual cocatalysts (Pt and Co polyoxometalate (POM)) modified TiO₂ was synthesized by electrostatic self-assembly and photodeposition methods. It shows a drastically elevated H₂O₂ yield of 0.93 mM h⁻¹ and concurrent HCOOH production rate at 0.46 mM h⁻¹. The X-ray photoelectron spectroscopy and theoretical calculations reveal that oxo-bridged POM leads to the electron redistribution of adjacent Pt and thus facilitates H₂O₂ desorption as well as retarding further decomposition. Simultaneously, deposited Co POM serves as the reservoir of photoelectrons and the bridge for electron transfer to metallic Pt through its ligand fragments. Lightweight polystyrene (PS) spheres enable the photocatalysts to float on a liquid surface with enhanced light utilization and intimate contact with gas reactants. This research not only furnishes insight into designing the highly-efficient photocatalytic system for hydrogen peroxide production but also explores the interaction between cocatalysts.

1. Introduction

As an eco-friendly oxidant and alternative energy carrier (1.72 MJ/kg in 50 wt% aqueous solutions), H₂O₂ is widely utilized in one-compartment fuel cells, chemical synthesis, and environmental remediation [1,2]. Currently, the anthraquinone method is the principal pathway for industrial production of H₂O₂, which is a highly energy-consuming process and emits toxic by-products [3,4]. An alternative route for the direct synthesis of H₂O₂ from the mixture of H₂ and O₂ catalyzed by noble metals or alloys faces the risk of explosion [5]. Thus, numerous endeavors are made to explore safe and cost-effective methods for H₂O₂ production. Thereinto, photocatalytic hydrogen peroxide generation has attracted extensive attention owing to its considerable merits in energy sustainability and environmental conservation [6–8].

Nonetheless, photocatalytic H₂O₂ production is still constrained by severe charge recombination, slow kinetics, and unfavorable H₂O₂ decomposition [9–11]. Though introducing hole scavengers can solve the above difficulties, undesirable oxidative products cause unnecessary

waste. Formic acid, serving as an indispensable intermediate in diverse chemical industries, has been widely utilized in direct formate fuel cells or hydrogen storage [12]. Consequently, oxidation of the simplest monohydric alcohol–methanol (\$350/t) to value-added formic acid (\$1300/t) is considered to be a profitable strategy in replacing scavenger oxidation.

In addition, the interfacial design of the photocatalytic system is of equal importance. Generally, agglomeration of catalysts, limited photoabsorption, recovery difficulty as well as sluggish delivery of gas reactants in traditional biphasic system hinder their further performance improvement [13–15]. Fortunately, the triphase system comprised of floatable photocatalysts can overcome the aforementioned problems [16,17]. Our preliminary work has demonstrated the effectiveness of the triphase system of floatable TiO₂/Bi₂O₃ photocatalyst for photocatalytic production of H₂O₂ and furoic acid [18,19]. The floatable photocatalyst maximizes light utilization and retains an adequate supply of oxygen in the triphase system, providing optimal choice for concurrent H₂O₂ production and conversion of organics.

Except for multiphase design and oxidative coupling to expedite

* Corresponding author.

** Corresponding author at: State Key Laboratory of Advanced Technology for Materials Synthesis and Processing, International School of Material Science and Engineering, Wuhan University of Technology, Wuhan 430070, PR China.

E-mail addresses: zhangliuyang@cug.edu.cn (L. Zhang), yujiaguo93@cug.edu.cn (J. Yu).

<https://doi.org/10.1016/j.apcatb.2022.122200>

Received 7 October 2022; Received in revised form 17 November 2022; Accepted 18 November 2022

Available online 19 November 2022

0926-3373/© 2022 Elsevier B.V. All rights reserved.

photocatalytic reaction, multifarious approaches are implemented for catalyst design, including surface modification [20–22], defect or doping engineering [23,24], and heterojunction construction [25–28]. Among these methods, cocatalysts modification can promote electron–hole separation, expedite the kinetics, provide additional active sites and simultaneously decelerate H_2O_2 decomposition [29–31]. Particularly, the loading of dual cocatalysts can endow the catalyst with exquisitely-designed functionalities [32–34]. Among multitudinous noble metal cocatalysts, platinum is exceptional as an electron sink due to its low Fermi level (1.1 V vs. NHE (normal hydrogen electrode)). However, the H_2O_2 molecule can easily chemisorb on Pt followed by the formation of $\text{Pt}(\text{O})$, and then H_2O_2 decomposes [35]. Thus, another cocatalyst needs to be added to regulate the H_2O_2 desorption on Pt and reduce the decomposition. As a mimicry of the natural enzyme, the Keggin-type $[\text{Co}_4(\text{H}_2\text{O})_2(\text{PW}_9\text{O}_{34})_2]^{10-}$ (Co-containing polyoxometalate, Co POM) consists of metal–oxo clusters with oxygen-enriched surfaces, which can modulate the electron density of Pt to facilitate the H_2O_2 desorption. Furthermore, robust all-inorganic ligand fragments in Co POM can encapsulate and protect active polynuclear transition metals [36,37]. The functional ligands with high-density oxygen atoms are capable to generate extended hydrogen bonding networks, and then the rapid, reversible and stepwise multiple electron transfer can proceed without structural changes [37,38].

Inspired by the previous work, the dual cocatalysts modified TiO_2 nanospheres are synthesized for photocatalytic H_2O_2 evolution via electrostatic self-assembly and photodeposition methods. Benefiting from the floatable photocatalyst, the sufficient supply of oxygen promotes the production of H_2O_2 . Besides, $\text{TiO}_2/\text{Pt}/\text{Co POM}$ shows the highest H_2O_2 production rates at 0.93 mM h^{-1} in four hours among TiO_2 (0.18 mM h^{-1}), $\text{TiO}_2/\text{Co POM}$ (0.50 mM h^{-1}) and TiO_2/Pt (0.20 mM h^{-1}). And, the corresponding HCOOH evolution rate of $\text{TiO}_2/\text{Pt}/\text{Co POM}$ can reach 0.46 mM h^{-1} , which is almost eight times higher than pristine TiO_2 . Synergistic effects of Co POM and Pt on modulating the photocatalytic performance and charge-carrier dynamics are systematically investigated through spectroscopic and electrochemical tests. Additionally, the electronic density around Pt can be modulated by the Co POM, facilitating newly formed H_2O_2 desorption and reducing its decomposition. The dual cocatalyst in the triphase system allows for a comprehensive investigation into the photocatalytic system design as well as synergistic effects between POM ligands and noble metals.

2. Experimental section

2.1. Synthesis of polystyrene (PS) nanosphere

According to the previously reported method, PS nanospheres were prepared as the template [39]. First of all, styrene was washed with 1 M NaOH three times to remove the polymerization inhibitor. 0.1 g of polyvinyl pyrrolidone (PVP) and 0.1026 g of ammonium persulfate (APS) were added to the mixture of 30 mL distilled water with 230 mL of ethanol, followed by stirring until a uniform solution was formed. After that, 22 mL of styrene monomer was dropped into the above solution and the polymerization was conducted in the oil bath at 70°C for 24 h. The reactor was cooled to room temperature by an ice bath, and then PS nanospheres were obtained by centrifugation and washed with H_2O and ethanol for six times.

2.2. Synthesis of TiO_2 nanosphere

TiO_2 precursor was first synthesized. 0.11 g of PS nanospheres were firstly added to 35 mL of ethanol to form a homogenous emulsion. Then, with the addition of 0.32 g of HDA and 0.8 mL of $\text{NH}_3\cdot\text{H}_2\text{O}$, the emulsion was sonicated and stirred for 15 min. Next, 0.2 mL of isopropyl titanate (IPT) was dropped into the dispersion with vigorous stirring for 1 h. The obtained sediment was washed with deionized water and ethanol alternatively and dried in a vacuum chamber at 60°C . At last, the white

powder was dispersed in the mixture of 50 mL of H_2O and 20 mL of ethanol followed by a hydrothermal process in an oven at 150°C for 12 h.

2.3. Synthesis of Co polyoxometalate (Co POM, $\text{Na}_{10}[\text{Co}_4(\text{H}_2\text{O})_2(\text{PW}_9\text{O}_{34})_2]$)

The preparation of $\text{Na}_{10}[\text{Co}_4(\text{H}_2\text{O})_2(\text{PW}_9\text{O}_{34})_2]$ was derived from formerly reported literature [40]. Briefly, 0.108 mol of $\text{Na}_2\text{WO}_4\cdot 2\text{H}_2\text{O}$, 0.012 mol of $\text{Na}_2\text{HPO}_4\cdot 7\text{H}_2\text{O}$, and 0.024 mol of $\text{Co}(\text{NO}_3)_2\cdot 6\text{H}_2\text{O}$ were dissolved with 100 mL of water in a three-neck round-bottom flask. After the pH was adjusted from 9 to 7 with 2 M HCl, the acquired purple suspension was maintained in an oil bath at 100°C and refluxed for two hours. Within minutes of heating, the solution gradually became dark purple. After the reflux process, the obtained solution was saturated with excessive NaCl and naturally cool to room temperature. The as-prepared purple crystals were collected, washed quickly with distilled water, and recrystallized from hot water.

2.4. Synthesis of $\text{TiO}_2/\text{Pt}/\text{Co POM}$ nanosphere

First, the 0.1 g of TiO_2 was ground into small particles followed by dispersion and sonication in 20 mL of deionized water. After the pH of the suspension was adjusted to 4.5, 0.02 g of Co POM was added by vigorous stirring. The $\text{TiO}_2/\text{Co POM}$ was obtained after the 12 h electrostatic self-assembly process. The Pt nanoparticles were finally dispersed homogeneously on the TiO_2 through the photoreduction of proportionate chloroplatinic acid (1.33 mg of $\text{H}_2\text{PtCl}_6\cdot\text{H}_2\text{O}$ for 50 mg of $\text{TiO}_2/\text{Co POM}$ sample). Ultimately, the $\text{TiO}_2/\text{Pt}/\text{Co POM}$ composite sample was washed by centrifugation and dried in a vacuum oven at 60°C for 12 h.

3. Results and discussion

3.1. Morphological and structural characterization

As shown in Fig. 1a, firstly, PS nanospheres are fabricated according to the previous method as the template for TiO_2 spheres. Then, by the addition of ammonia and hexadecylamine (HDA) surfactants, the hydrophilic amino group participates in the hydrolysis of $\text{Ti}(\text{OC}_3\text{H}_7)_4$ through hydrogen-bonding interactions, forming the TiO_2 -precursor inorganic-organic layer [41]. After the hydrothermal treatment, TiO_2 nanocrystals form on PS spheres by removing organic species. In Fig. 1b, the Zeta potentials of TiO_2 nanosphere and Co POM are tested. Under the pH of 4.5, TiO_2 and Co POM show the opposite Zeta potential. Hence, the $\text{TiO}_2/\text{Co POM}$ can be synthesized by the electrostatic self-assembly method in the aqueous solution at pH = 4.5. Afterwards, 1%wt metallic Pt is deposited on the Co POM via the photoreduction method. Additionally, the actual loading ratio of Co POM is tested to be approximately 15% through inductively coupled plasma-atomic emission spectrometry (ICP-AES).

In Fig. 1c, X-ray diffraction (XRD) patterns are obtained to analyze the crystal structure of all the catalysts. The sharp diffraction peaks are assigned to the anatase TiO_2 phase (JCPDS, No. 99-0008), indicating the growth of high-crystallinity TiO_2 . And, the broad peak located at 20° is ascribed to the PS template. Meanwhile, the coexistence of heart-symbol labeled peaks of Co POM elucidates its successful introduction. On account of the low loading weight, the peak of metallic Pt cannot be found in the XRD patterns.

As observed in Fig. S1a (Supporting Information), the pristine TiO_2 shows good hydrophobicity with a water contact angle of 110.8° due to its surface alkylation. After the loading of cocatalysts, all the contact angles are slightly reduced but decent hydrophobicity is still preserved. Besides, with the assistance of light-weight PS spheres, powdery $\text{TiO}_2/\text{Pt}/\text{Co POM}$ can float on the liquid surface (in Fig. 1d and e). The floatable photocatalyst enables intimate contact with both O_2 and water

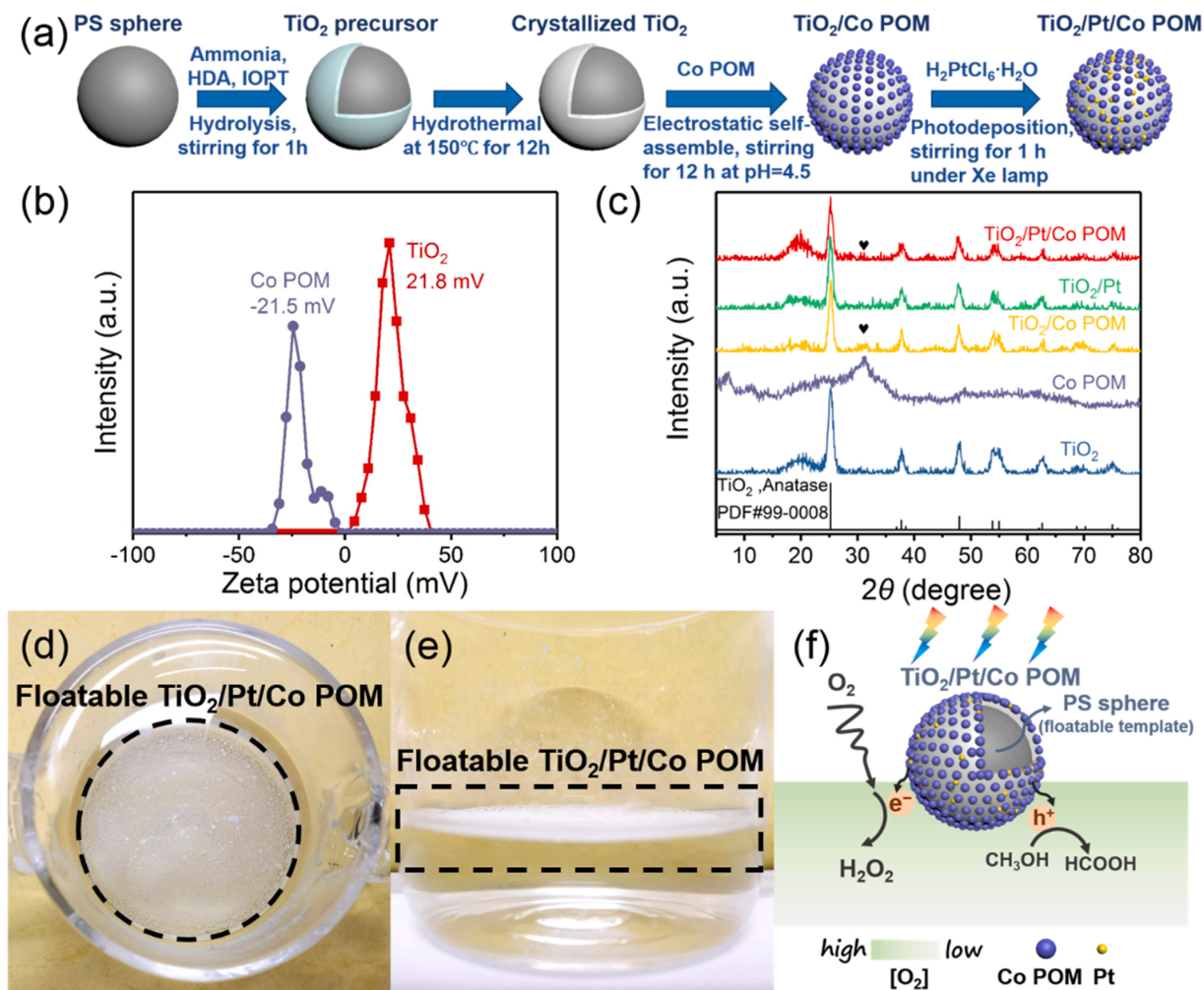


Fig. 1. (a) Schematic illustration of the synthetic process of TiO₂/Pt/Co POM nanospheres. (b) Zeta potentials of TiO₂ and Co POM tested at the pH of 4.5. (c) XRD patterns of as-prepared TiO₂, TiO₂/Co POM, TiO₂/Pt and TiO₂/Pt/Co POM. (d–e) Top and side views of the floatable TiO₂/Pt/Co POM. (f) Schematic illustration of H₂O₂-production in the triphase system.

synchronously, thus resulting in the coexistence of gas–solid–liquid tri-phase at the micro/nanoscale level. As illustrated in Fig. 1f, the floatable TiO₂/Pt/Co POM maximizes the absorption of incident light. In the traditional liquid–solid system, the oxygen dissolves in the water

with a gradient at a low concentration (8.38 mg/L at 25 °C). Thus, the aerobic reaction suffers from sluggish kinetics due to the lack of O₂. Distinctively, at the gas–solid–liquid interface, abundant O₂ firstly adsorbs on the Pt active sites and then is reduced to H₂O₂ by

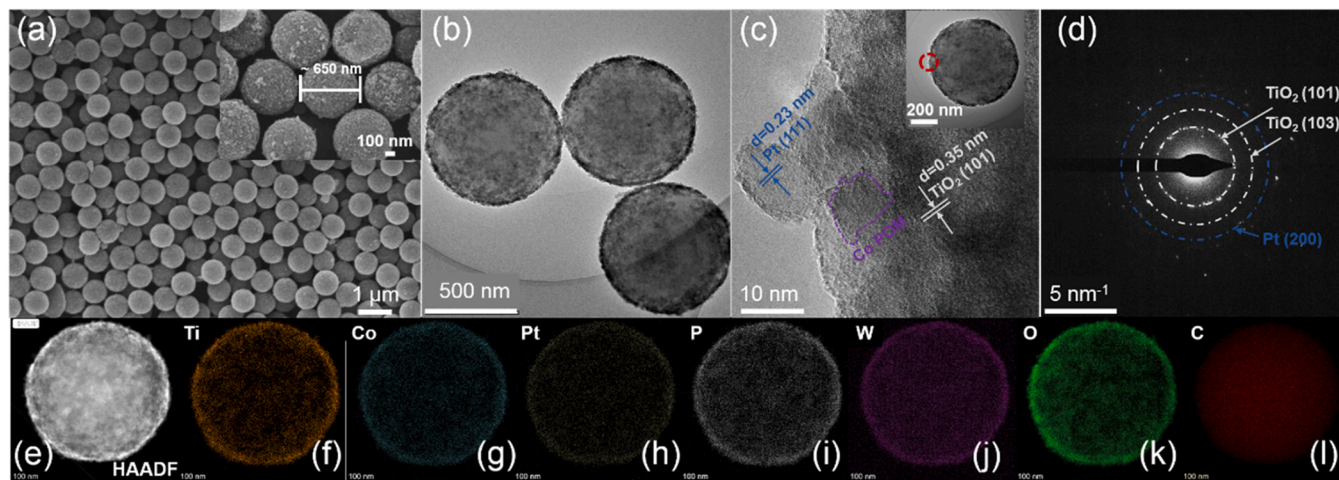


Fig. 2. (a) FESEM image of TiO₂/Pt/Co POM at low magnification (inset: its high magnification image). (b) TEM and (c) HRTEM images (inset: the selected area), (d) SAED pattern, (e) HAADF and (f–l) element distribution maps of TiO₂/Pt/Co POM.

photogenerated electrons. Simultaneously, holes oxidize the methanol to accelerate charge separation.

As depicted in Fig. 2a and S2a–f, the morphologies of all the samples are acquired on the field-emission scanning electron microscopy (FESEM). PS spheres show a smooth surface with an average diameter of about 500 nm (in Fig. S2a). As observed in Fig. S2b, the amorphous precursor of TiO₂ shows a rough surface with multiple pits. This is ascribed to the hydrophobic long chains of hexadecylamine molecule which can self-assemble into the rod-like micelles and create pores in the TiO₂-precursor [41]. After the hydrothermal process, in Fig. S2c, the amorphous TiO₂ precursor crystallizes into TiO₂ nanocrystal layer on the surface. After the loading of Co POM and Pt nanoparticles, the original nanosphere morphology is maintained (in Fig. S2d–f). Moreover, Fig. 2a and the inset show the homogeneously dispersed spheres of TiO₂/Pt/Co POM with an approximate diameter of 650 nm. As presented in Fig. 2b, the transmission electron microscopy (TEM) image indicates the core-shell structure of TiO₂/Pt/Co POM nanosphere with a shell thickness of about 60 nm. From the high-resolution TEM (HRTEM) image and selected area electron diffraction (SAED) pattern, the clear lattice fringe and diffraction rings can be observed. In Fig. 2c, the interplanar distances of 0.23 nm and 0.35 nm are ascribed to the (111) plane of Pt and (101) plane of TiO₂, respectively. Some particles without lattice fringe correspond to the Co POM with poor crystallinity. In addition, the two inner diffraction rings in Fig. 2d match well with the (101) and (103) planes of anatase TiO₂. And, the outer one belongs to the (200) facet of metallic Pt. The high-angle annular dark-field (HAADF) image (Fig. 2e) and the corresponding energy-dispersive X-ray spectroscopy (EDS) (Fig. 2f–l) mapping patterns confirm the core-shell structure and uniform distribution of Ti, Co, Pt, P, W, O and C. Specifically, C distributes in the inner area implies the core of PS sphere. And the rest elements mainly disperse on the outer shell, indicating the successful synthesis of TiO₂ layer with scattered dual cocatalysts.

3.2. Characterization of optical properties

The optical absorption properties of as-prepared samples are studied utilizing UV–vis diffuse reflectance spectroscopy (Fig. S3). The pristine TiO₂ exhibits an intrinsic absorption edge at around 380 nm, corresponding to a bandgap (E_g) of 3.26 eV. Due to the existence of polytungstate ligands in Keggin-type POM, a broad ligand-to-metal charge-transfer (LMCT) absorption band emerges at around 530 nm, leading to the slight redshift in absorbance edges of TiO₂/Co POM and TiO₂/Pt/Co POM [42]. With the coupling of Pt, TiO₂/Pt exhibits an intensified absorption from 400 nm to 800 nm without altering the light absorption edge.

3.3. Photocatalytic H₂O₂ production, decomposition and stability tests

Photocatalytic H₂O₂-production tests are conducted in 30 mL oxygen-saturated methanol (MeOH, 2 mM) solution irradiated with a 5 W lamp for 4 h (light wavelength: 365 nm). In Fig. 3a, compared with pristine TiO₂ (0.72 mM), the H₂O₂-yield of TiO₂/Co POM reaches 2.00 mM in four hours. For TiO₂/Pt, photodeposited Pt slightly speeds up the evolution of H₂O₂ and the yield is elevated to 0.79 mM. When Co POM and Pt are deposited on the TiO₂ simultaneously, the production substantially increases to 3.72 mM, which is approximately five-fold of pristine TiO₂. For the evaluation of H₂O₂ activity, the apparent quantum yield (AQY) of TiO₂/Pt/Co POM is calculated to be 1.09%.

Photocatalytic H₂O₂ evolution proceeds through two competitive reactions, i.e. formation and decomposition. In consequence, a kinetic model is developed for the evaluation of zero-order and first-order in H₂O₂ formation and H₂O₂ decomposition (as shown in Eq. 1) [43]:

$$[H_2O_2] = \frac{K_f}{K_d} (1 - e^{-K_d t}) \quad (1)$$

K_f (mmol L⁻¹ h⁻¹) and K_d (h⁻¹) represent the formation and decomposition rate constants, respectively. According to previous research, Ti-OOH complex forms on the surface of TiO₂ due to the

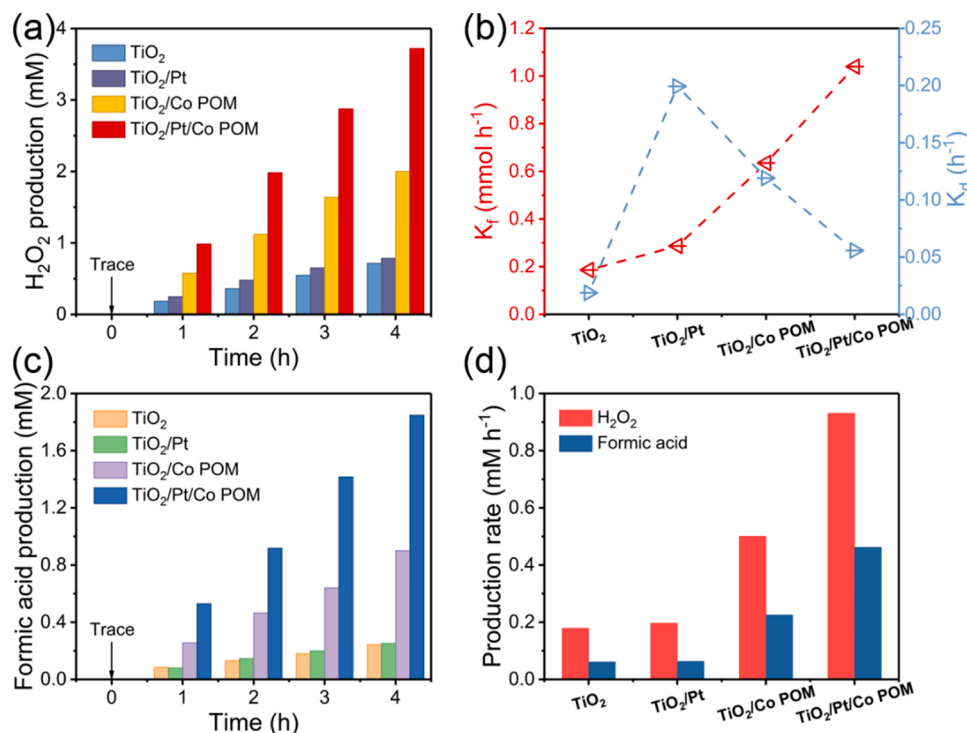


Fig. 3. (a) Photocatalytic H₂O₂ evolution in O₂-saturated aqueous solution of methanol under 5 W 365 nm-LED lamp-illumination in 4 h and (b) the fitted formation rate constant (K_f) and decomposition rate constant (K_d) of TiO₂, TiO₂/Co POM, TiO₂/Pt and TiO₂/Pt/Co POM. (c) Photocatalytic HCOOH production in 4 h and (d) the corresponding production rates.

adsorption of formed H_2O_2 . Generally, Ti-OOH induces the decomposition of the H_2O_2 ($\text{Ti-OOH} + \text{H}^+ + \text{e}^- \rightarrow \text{Ti-OH} + \text{OH}^-$) and renders the low yield [44]. Therefore, in Fig. 3b, the K_f and K_d for TiO_2 are small. As previously reported, Pt(O) forms with the adsorption of H_2O_2 and ultimately boost the decomposition process ($\text{Pt(O)} + \text{H}_2\text{O}_2 \rightarrow \text{Pt} + \text{O}_2 + \text{H}_2\text{O}$) [45]. Hence, TiO_2/Pt shows the highest rate of decomposition (0.20 h^{-1}) among all the samples. For $\text{TiO}_2/\text{Pt/Co POM}$, contrary to the adverse effect of Pt in TiO_2 as mentioned before, K_d is 0.055 h^{-1} and K_f reaches $1.04 \text{ mmol L}^{-1} \text{ h}^{-1}$. This is ascribed to the facile electron conduction via Co POM derived from its oxobridged complex [46].

The HCOOH production is evaluated simultaneously with H_2O_2 evolution. As depicted in Fig. 3c, after reacting for 4 h, dual-cocatalysts-coated TiO_2 produces 1.85 mM HCOOH , which is much higher than pristine TiO_2 (0.24 mM). Besides, the conversion efficiency can reach 99% in 4 h and selectivity exceeds 92.5%. In Fig. 3d, TiO_2 shows the HCOOH production rate at 0.06 mM h^{-1} , which is lower than TiO_2/Pt (0.063 mM h^{-1}) and $\text{TiO}_2/\text{Co POM}$ (0.225 mM h^{-1}). As expected, $\text{TiO}_2/\text{Pt/Co POM}$ exhibits the highest HCOOH production rate at 0.46 mM h^{-1} , and the corresponding H_2O_2 production rate is 0.93 mM h^{-1} . Furthermore, the reaction product of $\text{TiO}_2/\text{Pt/Co POM}$ is analyzed by gas chromatography-mass spectrometry (GC-MS) and the spectra are shown in Fig. S4. The mass spectrum accords quite well with standard HCOOH , which is consistent with previous HPLC results. In order to verify the good stability of $\text{TiO}_2/\text{Pt/Co POM}$ in photocatalytic process, the XRD patterns and FESEM images of catalysts after photocatalytic tests are conducted. As depicted Fig. S5, the distinct XRD peaks barely change, and the microsphere morphology is retained except for slight adhesion.

3.4. Characterization of charge separation ability

For the evaluation of photoelectron transfer capability, electrochemical impedance spectra (EIS) are tested at -0.3 V vs. Ag/AgCl under light irradiation. The Nyquist plots (Fig. 4a) supply adequate evidence that R_{ct} in $\text{TiO}_2/\text{Pt/Co POM}$ is the lowest, corresponding to the remarkable bulk-to-surface electron transfer ability [47]. Besides, in Fig. S6a, the photocurrent of TiO_2 is only $0.2 \mu\text{A cm}^{-2}$. After loading

single cocatalyst, the photocurrents elevate about two or three times. And, the current density of Pt and Co POM co-modified TiO_2 can reach $1.2 \mu\text{A cm}^{-2}$ as expected, which is almost six times higher than that of pristine TiO_2 . The steady-state fluorescence tests of all the samples (in Fig. S6b) suggests that the modification of dual cocatalyst is effective in suppressing charge carrier recombination. To analyze the photo-generated charge migration and recombination dynamics, time-resolved PL (TRPL) spectra are employed. After fitting the curves in Fig. 4b and obtaining the parameters in Table 1, τ_1 refers to the radiative recombination of photoexcited e^- and h^+ that leads to the fluorescence emission of TiO_2 -based samples. Among all the samples, $\text{TiO}_2/\text{Pt/Co POM}$ has a minimum τ_1 of 0.71 ns , originating from the reduced radiative recombination and enhanced photogenerated charge transfer via LMCT channel to the anchored Pt [48,49]. Consistent with the analysis above, the shortened average lifetime (τ_a) of $\text{TiO}_2/\text{Pt/Co POM}$ compared with TiO_2 also implies the effective charge separation and transfer from TiO_2 to the loaded Co POM and Pt nanoparticles [50].

3.5. Elucidation of photocatalytic formation pathway of H_2O_2 and HCOOH

To clarify the route of O_2 reduction reaction (ORR), the number of transferred electrons is measured by the rotating disk electrode (RDE) test. As depicted in Fig. S7, the linear sweep voltammetry curves of all the samples are tested in $0.1 \text{ mol/L NaClO}_4$ solution (adjusted to $\text{pH}=4$)

Table 1

Triple exponential fitted results of τ_1 , τ_2 and τ_3 , corresponding percentage contributions and calculated τ_a .

	τ_1 (ns)	Rel. %	τ_2 (ns)	Rel. %	τ_3 (ns)	Rel. %	τ_a (ns)
TiO_2	0.92	12.43	3.90	53.54	14.76	34.03	7.23
$\text{TiO}_2/\text{Co POM}$	0.86	20.87	3.35	51.74	12.09	27.40	5.23
TiO_2/Pt	0.73	16.72	3.51	49.55	14.98	33.72	6.92
$\text{TiO}_2/\text{Pt/Co POM}$	0.71	13.97	3.62	54.21	13.65	31.82	6.41

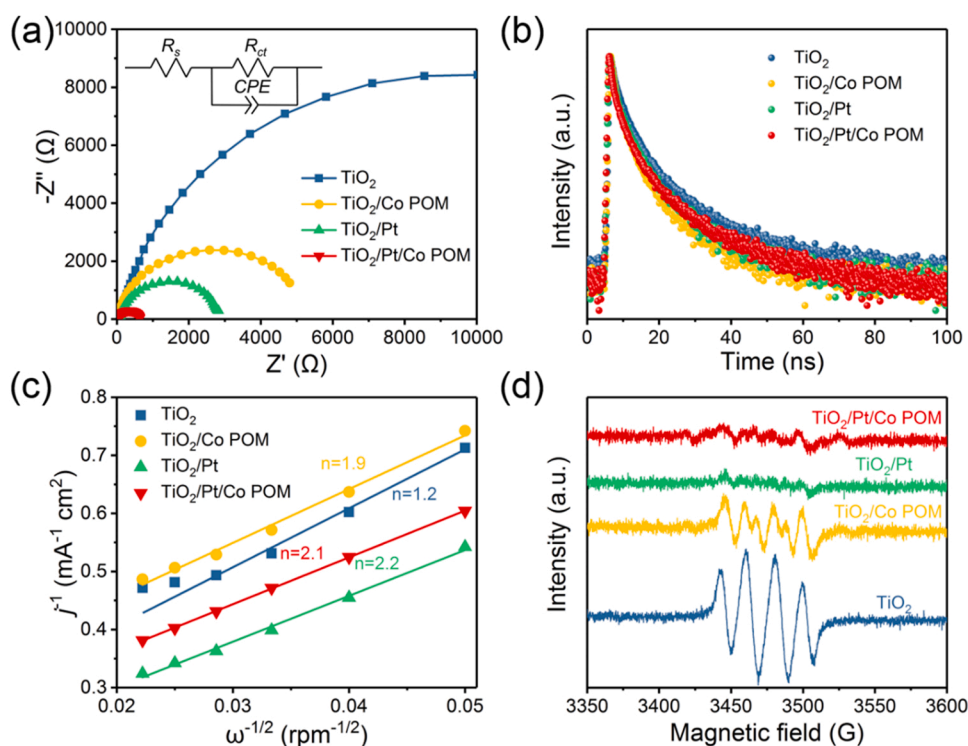


Fig. 4. (a) Nyquist plots tested in Na_2SO_4 aqueous solution at -0.3 V vs. Ag/AgCl tested with illumination (inset: equivalent circuit of TiO_2 -derived photocatalysts, in which R_s is solution resistance, R_{ct} represents the resistance of charge transfer and CPE is the constant phase element in the catalyst), (b) TRPL spectra, (c) Koutecky-Levich plots fitted with different rotating speeds at -0.57 V vs. RHE and (d) EPR spectra of DMPO-O_2^- for TiO_2 , $\text{TiO}_2/\text{Co POM}$, TiO_2/Pt and $\text{TiO}_2/\text{Pt/Co POM}$.

at different rotating speeds. After the loading of Co POM, a slight increase of maximum current density at different rotating speeds can be observed. Whereas, with the photodeposited Pt nanoparticles, the maximum current density of TiO₂/Pt and TiO₂/Pt/Co POM are both improved, owing to the remarkable reduction capability of Pt. Furthermore, the Koutecky–Levich plots are fitted (in Fig. 4c) and the average number of electrons transfer (n) involved in ORR is calculated by the linear regression employing Eqs. (2 and 3) below [51]:

$$j^{-1} = j_k^{-1} + B^{-1} \omega^{-1/2} \quad (2)$$

$$B = 0.2nF\nu^{-1/6}CD^{2/3} \quad (3)$$

in which j represents the measured current density, j_k refers to the kinetic current density, ω is the rotating speed (rpm), F represents the Faraday constant (96,485 C mol⁻¹), and C represents the bulk concentration of oxygen in water (1.26×10^{-3} mol cm⁻³), ν is hydrodynamic viscosity of water (0.01 cm² s⁻¹) and D refers to the diffusion coefficient of oxygen (2.7×10^{-5} cm² s⁻¹), respectively. According to the equations above, the number of transferred charges is calculated to be 1.2 of TiO₂, implying the multi-step consecutive single-electron ORR pathway (in Eqs. 4 and 5) in TiO₂ [52]. Whereas, the n values for TiO₂/Co POM, TiO₂/Pt and TiO₂/Pt/Co POM are fitted to be 1.9, 2.2 and 2.1, respectively. This result suggests that, in the presence of cocatalysts, one-step two-electron O₂ reduction (in Eq. 6) dominates. Namely, the ORR pathway can be altered by the deposition of cocatalysts.



Fig. 4d shows the electron paramagnetic resonance (EPR) spectroscopy of DMPO- $\bullet O_2^-$ adduct for TiO₂ and TiO₂ modified with cocatalysts. The strongest DMPO- $\bullet O_2^-$ signal can be observed for TiO₂, because the oxidation potential of photoexcited electrons in the CB of TiO₂ is higher than that of O₂/ $\bullet O_2^-$. Meanwhile, this also shows that the H₂O₂ production on TiO₂ is dominated by a one-electron pathway. The suppressed signal of the typical intermediate in TiO₂/Co POM and TiO₂/Pt indicates a less possible one-electron ORR pathway. Consistent with the mentioned above, the dominated one-step two-electron O₂ reduction process can account for the barely identifiable signal of TiO₂/Pt/Co POM. Besides, p-benzoquinone (BQ), isopropanol (IPA) and triethanolamine (TEOA) are added as arresters for $\bullet O_2^-$, $\bullet OH$ and h^+ respectively in trapping tests (in Fig. S8). After the addition of BQ, the H₂O₂ yield over TiO₂/Co POM, TiO₂/Pt and TiO₂/Pt/Co POM reduces over 90%, implying the main contribution of $\bullet O_2^-$ in H₂O₂ production. In $\bullet OH$ and h^+ trapping experiments, H₂O₂ productions have no significant change compared with that of methanol. The results also reinforce the O₂ reduction to H₂O₂.

In situ diffuse-reflectance infrared Fourier transform spectroscopy (DRIFTS) is employed to detect organic intermediates during CH₃OH oxidation process. Initially, CH₃OH gas is introduced and the molecules are adsorbed on TiO₂ in dark conditions. In Fig. 5a, the broad negative peak at 3334 cm⁻¹ is assigned to the adsorbed H₂O and stretching vibration of -OH in CH₃OH. The C-O stretching vibration peak emerges at

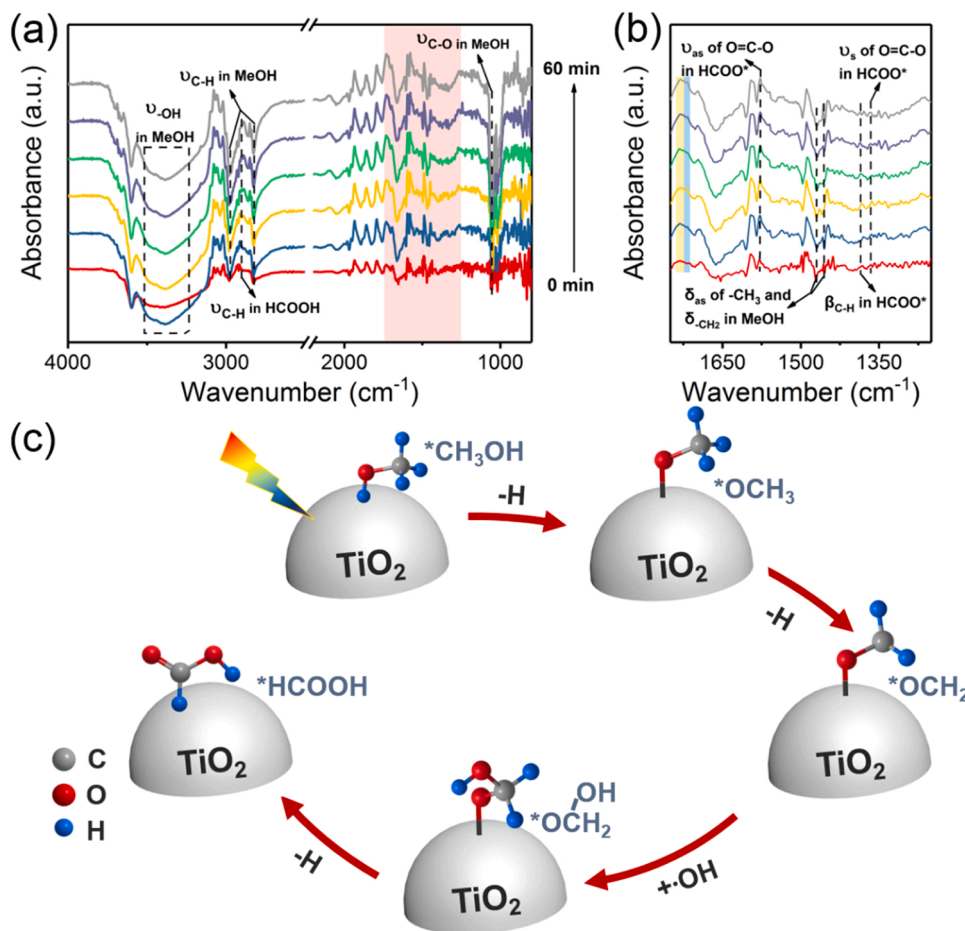


Fig. 5. (a) *In situ* DRIFT spectra of TiO₂/Pt/Co POM tested under light for 60 min with interval of 10 min (b) The detailed view of the red marked area from 1750 to 1250 cm⁻¹ in DRIFT spectra. (c) The photocatalytic CH₃OH oxidation mechanism on TiO₂ surface.

1054 cm^{-1} . Another two peaks located at 1455 and 1469 cm^{-1} are ascribed to the bending vibration of methyl and methylene groups (in Fig. 5b). The stretch vibration peaks of C–H are at 2830 and 2980 cm^{-1} , respectively. All the negative peaks intensify over time, indicating the gradually increased CH_3OH consumption. Meanwhile, the newly formed peaks of aldehyde carbonyl at 1728 cm^{-1} (highlighted with yellow) suggest that formaldehyde acts as the oxidative intermediate. Afterwards, the symmetry and asymmetry stretching vibration peaks of $\text{O}=\text{C}-\text{O}$ situated at 1369 and 1572 cm^{-1} (in Fig. 5b) are attributed to carboxy carbonyl in HCOOH , indicating the conversion from formaldehyde. These peaks also intensify with the accumulation of formed formic acid. According to the analysis above, the supposed mechanism of MOR is summarized in Fig. 5c. Firstly, the CH_3OH molecule deprotonates to form $\text{CH}_3\text{O}^\bullet$ radical. Then, the $\text{CH}_3\text{O}^\bullet$ radicals can be captured by DMPO and detected by an EPR spectrometer (in Fig. S9). Subsequently, $\text{CH}_3\text{O}^\bullet$ deprotonates ulteriorly and reacts with $^\bullet\text{OH}$ to generate $\text{CH}_2(\text{OH})\text{O}^\bullet$. Ultimately, HCOOH can be obtained through dehydrogenation of $\text{CH}_2(\text{OH})\text{O}^\bullet$.

3.6. X-ray photoelectron spectroscopy analysis

X-ray photoelectron spectroscopy (XPS) is acquired to reveal the electron density change in some of the elements. The peaks at 458.6 and 464.5 eV belong to $\text{Ti } 2p_{3/2}$ and $\text{Ti } 2p_{1/2}$ in the $\text{Ti } 2p$ XPS spectrum of TiO_2 (Fig. 6a). And, the $\text{Ti } 2p$ peaks in $\text{TiO}_2/\text{Co POM}$, TiO_2/Pt and $\text{TiO}_2/\text{Pt/Co POM}$ migrate to the higher binding energy, indicating the decreased electron density in TiO_2 . As observed in Fig. 6b, the $2p_{3/2}$ and $2p_{1/2}$ peaks of Co in high-resolution spectrum of $\text{TiO}_2/\text{Co POM}$, decrease to 781.7 and 791.6 eV compared to that of Co POM. The negative shift corroborates the electron transfer from TiO_2 to Co POM. However, the peaks of $\text{TiO}_2/\text{Pt/Co POM}$ shift to the higher binding energy compared with $\text{TiO}_2/\text{Co POM}$, implying the electron transfer from Co POM to Pt. Additionally, in Fig. 6c, the 4f peaks of Pt in $\text{TiO}_2/\text{Pt/Co POM}$ migrate to lower binding energy than that of $\text{TiO}_2/\text{Co POM}$, which further confirms the electron transfer from TiO_2 to Pt via Co POM [53]. The O 1s spectra of TiO_2 shown in Fig. S10 can be deconvoluted into peaks of lattice oxygen, hydroxyl groups and adsorbed H_2O situated at

529.6, 531.2 and 533.2 eV, respectively. Compared with those in TiO_2 , the three peaks of O in Co POM migrate to the higher binding energy because of the larger electronegativity of Ti compared to Co.[54] Therefore, the binding energy of three peaks in $\text{TiO}_2/\text{Co POM}$ and $\text{TiO}_2/\text{Pt/Co POM}$ is higher than that in TiO_2 as well. As illustrated in Fig. 6d, the peak positions of $\text{W } 4f_{5/2}$ and $\text{W } 4f_{7/2}$ in $\text{TiO}_2/\text{Co POM}$ and $\text{TiO}_2/\text{Pt/Co POM}$ shift positively compared with pristine Co POM because of the drift of electrons from W to Co ion. Further observation reveals a newly emerged peak at 34.3 eV, signifying the partial electronic redistribution in Keggin cluster ($[\text{PW}_9\text{O}_{34}]^{9-}$) in Co POM, probably because the W-centered LUMOs (lowest unoccupied molecular orbitals) receive some electrons from O^{2-} . [55] Meanwhile, the interior charge redistribution leads to the formation of the electron trap center in Co POM, which benefits the charge transport process to Pt active sites through Keggin-type ligand.

3.7. Mechanism discussion on photocatalytic enhancement

DFT calculations are employed for in-depth investigation of the H_2O_2 process on dual or single cocatalysts modified TiO_2 . For further analysis of the kinetic process, the free energy in multiple steps for H_2O_2 evolution is calculated and the optimized structures are depicted in Fig. 7a. Concerning $\text{TiO}_2/\text{Pt/Co POM}$, the O_2 molecule is firstly adsorbed on the Pt cluster spontaneously with the free energy (ΔG) of -1.58 eV. Immediately after protonation, the adsorbed oxygen transforms to $^\bullet\text{OOH}$ with a downhill process. Ultimately, with further protonation to $^\bullet\text{HOOH}$, the final HOOH desorption process is a rate-determining step for H_2O_2 production. The desorption step on $\text{TiO}_2/\text{Pt/Co POM}$ is an uphill reaction with ΔG of 0.22 eV. But it is more favorable than the reaction over TiO_2/Pt (2.67 eV) as predicted. Furthermore, easier desorption of H_2O_2 also demonstrates that the electron-delocalized interaction between platinum and POM results in changes in interfacial electronic distribution and thus affects the desorption force of hydrogen peroxide at the surface of Pt. Hence, in Fig. 7b, O_2 molecules adsorb on Pt sites and receive electrons from Co POM followed by H_2O_2 evolution and further desorption. Parallely, holes oxidize the methanol to achieve higher charge separation

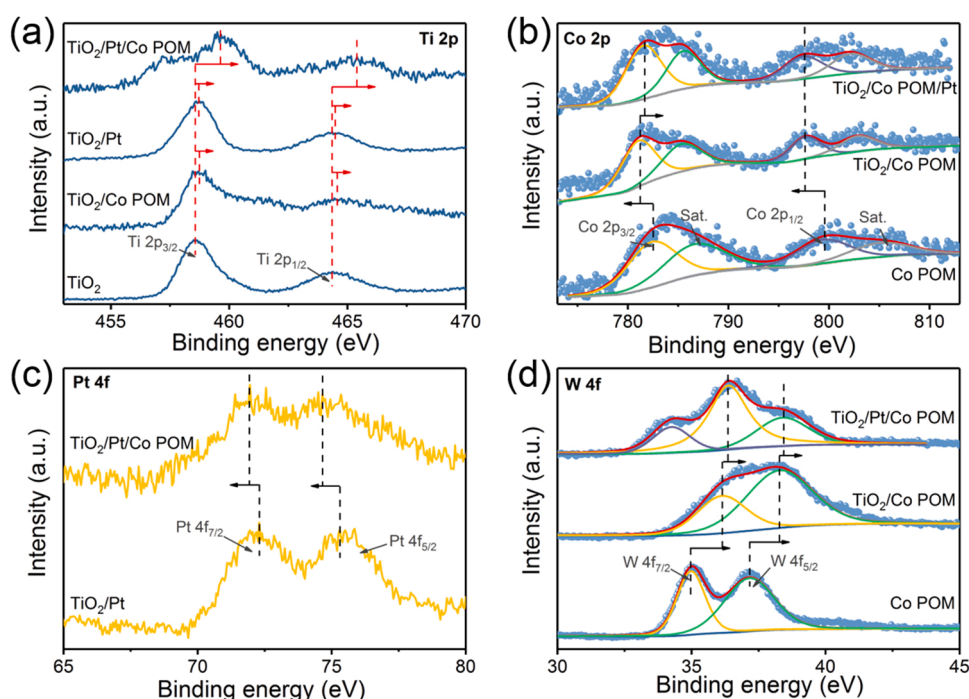


Fig. 6. High-resolution XPS spectra of (a) $\text{Ti } 2p$ in TiO_2 , TiO_2/Pt , $\text{TiO}_2/\text{Co POM}$ and $\text{TiO}_2/\text{Pt/Co POM}$; (b) $\text{Co } 2p$ in Co POM, $\text{TiO}_2/\text{Co POM}$ and $\text{TiO}_2/\text{Pt/Co POM}$; (c) $\text{Pt } 4f$ in TiO_2/Pt and $\text{TiO}_2/\text{Pt/Co POM}$; (d) $\text{W } 4f$ in Co POM, $\text{TiO}_2/\text{Co POM}$ and $\text{TiO}_2/\text{Pt/Co POM}$.

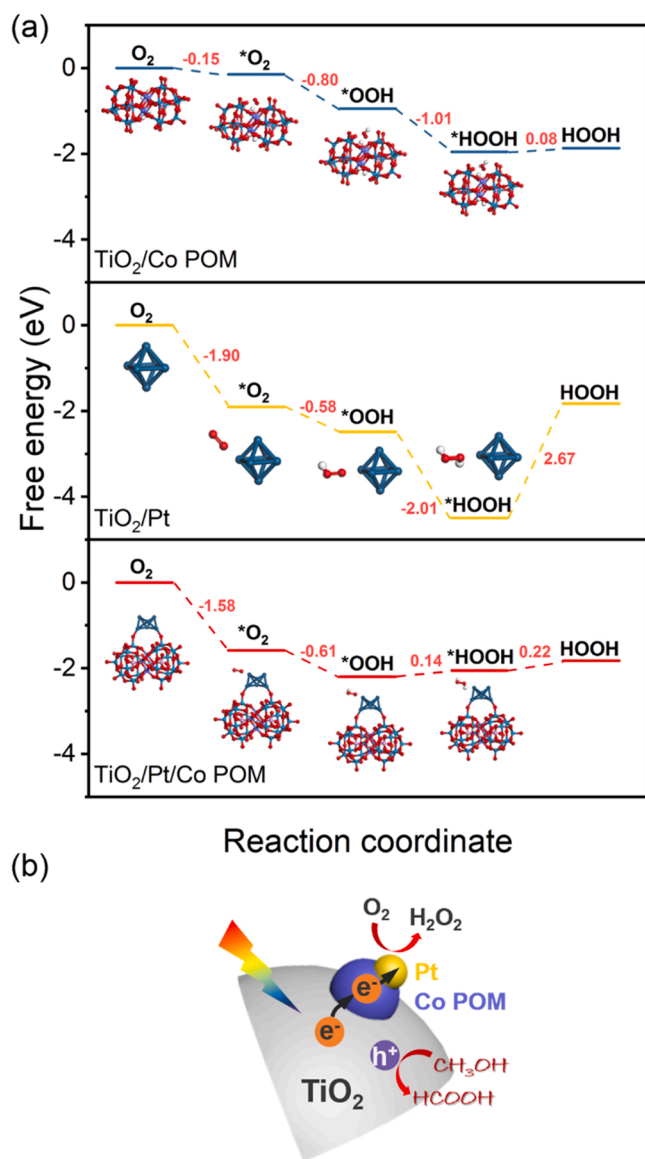


Fig. 7. (a) Free energy diagrams of oxygen reduction steps on active sites (*) of TiO₂/Pt/Co POM. (b) Schematic of redox reactions at TiO₂/Pt/Co POM under light illumination.

efficiency.

Mott–Schottky (M–S) and work function (WF) tests are conducted to investigate the band structures of all the samples. As shown in Fig. S11, the slopes of all the samples are positive, indicative of their n-type features. And, the flat band of TiO₂ situates at -0.4 V vs. NHE, pH = 0. The contact potential difference (CPD) is measured via the Kelvin probe to quantitatively calculate the work functions (WFs) (in Fig. S12). Work functions are determined by the Eq. (7) presented below:

$$W_{\text{sample}} = e \times \text{CPD}_{\text{sample}} + W_{\text{probe}}, \quad (7)$$

where $\text{CPD}_{\text{sample}}$ represents the CPD of the sample under test, and W_{probe} refers to the work function of Au probe (4.25 eV). The measured CPD values of TiO₂ and Co POM in the absence of light are 391.2 and 493.5 mV (in Table S1) with their corresponding WFs at 4.64 and 4.74 eV. With 369 nm-light, the CPD value of TiO₂ shows an obvious decrease, re-testifying its n-type semiconductor character. However, the contact potential difference of Co POM remains unchanged, which is non-responsive to illumination, implying its metal-like property. In Fig. 8a, the Fermi level (E_f) of Pt is lower than that of Co POM and TiO₂. Then, when the multi-junction is constructed, electrons in TiO₂ will flow to Co POM at first, and then transfer to Pt. The E_f of TiO₂ in the interface region gradually bends until the Fermi levels equilibrium is realized at the exact contacting point while the E_f of bulk remains unchanged (Fig. 8b). Under light illumination with a wavelength of 369 nm, the CPDs of all the samples, except for Co POM, show decreasing trends. Hence, as shown in Fig. 8c, the higher E_f of TiO₂ under illumination induces further electron transfer to Co POM and Pt.

4. Conclusions

To summarize, a ternary TiO₂/Pt/Co POM floatable photocatalyst is meticulously designed and synthesized. By introducing the triphase photocatalytic system, sufficient O₂ and illumination can participate in photocatalytic reactions without hindrance over the floatable photocatalyst. Meanwhile, Co POM and Pt co-coated TiO₂ nanospheres exhibit the highest photocatalytic H₂O₂ generation rates at 0.93 mM h^{-1} and the simultaneous HCOOH evolution rate at 0.46 mM h^{-1} . Co POM serves as a channel for electrons transfer to the Pt sites through ligand networks. TRPL and photochemical tests demonstrate the significantly accelerated electron-hole migration and effectively reduced charge carriers recombination compared with the single cocatalyst-modified counterparts. Furthermore, XPS analysis and theoretical calculations imply that POM helps the electronic redistribution around Pt, thus facilitating the H₂O₂ desorption step to retard the H₂O₂ decomposition. This research corroborates the potential of dual-cocatalyst for enhancement in photocatalytic H₂O₂ evolution and other applications.

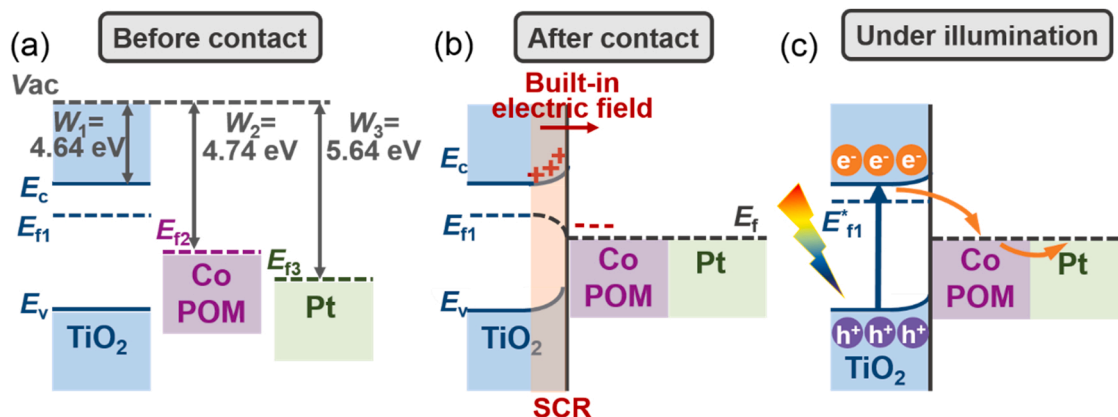


Fig. 8. Fermi levels (or WFs) and electron transfer mechanism among TiO₂, Co POM, and Pt (a) before contact, (b) after contact, and (c) under light illumination.

CRediT authorship contribution statement

Bowen He: Conceptualization, Data curation, Formal analysis, Methodology, Writing – original draft. **Cheng Luo:** Methodology, Data curation, Software. **Zhongliao Wang:** Methodology, Data curation, Software. **Liuyang Zhang:** Conceptualization, Funding acquisition, Resources, Project administration, Supervision, Writing – review & editing. **Jiaguo Yu:** Conceptualization, Formal analysis, Funding acquisition, Resources, Project administration, Supervision, Writing – review & editing.

Declaration of Competing Interest

The authors declare that they have no known competing financial interests or personal relationships that could have appeared to influence the work reported in this paper.

Data Availability

Data will be made available on request.

Acknowledgements

This work was supported by the National Natural Science Foundation of China (NSFC) (Nos. 52073223, 22278383, 51872220, 51932007, 22238009, 21871217 and U1905215).

Appendix A. Supporting information

Supplementary data associated with this article can be found in the online version at doi:10.1016/j.apcatb.2022.122200.

References

- [1] C. Xia, Y. Xia, P. Zhu, L. Fan, H. Wang, Direct electrosynthesis of pure aqueous H₂O₂ solutions up to 20% by weight using a solid electrolyte, *Science* 366 (2019) 226–231.
- [2] J. Gao, H. Yang, X. Huang, S. Hung, W. Cai, C. Jia, S. Miao, H. Chen, X. Yang, Y. Huang, T. Zhang, B. Liu, Enabling direct H₂O₂ production in acidic media through rational design of transition metal single atom catalyst, *Chem* 6 (2020) 658–674.
- [3] Y. Wang, G.L.N. Waterhouse, L. Shang, T. Zhang, Electrocatalytic oxygen reduction to hydrogen peroxide: from homogenous to heterogenous electrocatalysis, *Adv. Energy Mater.* 11 (2021) 2003323.
- [4] B. Liu, C. Bie, Y. Zhang, L. Wang, Y. Li, J. Yu, Hierarchically porous ZnO/g-C₃N₄ S-scheme heterojunction photocatalyst for efficient H₂O₂ production, *Langmuir* 37 (2021) 14114–14124.
- [5] L. Wang, J. Zhang, Y. Zhang, H. Yu, Y. Qu, J. Yu, Inorganic metal-oxide photocatalyst for H₂O₂ production, *Small* 18 (2022) 2104561.
- [6] C. Krishnaraj, H. Sekhar Jena, L. Bourda, A. Laemont, P. Pachfule, J. Roeser, C. V. Chandran, S. Borgmans, S.M.J. Rogge, K. Leus, C.V. Stevens, J.A. Martens, V. Van Speybroeck, E. Breynaert, A. Thomas, P. Van Der Voort, Strongly reducing (diarylamino)benzene-based covalent organic framework for metal-free visible light photocatalytic H₂O₂ generation, *J. Am. Chem. Soc.* 142 (2020) 20107–20116.
- [7] C. Pan, G. Bian, Y. Zhang, Y. Lou, Y. Zhang, Y. Dong, J. Xu, Y. Zhu, Efficient and stable H₂O₂ production from H₂O and O₂ on BiPO₄ photocatalyst, *Appl. Catal. B* 316 (2022), 121675.
- [8] J. Luo, C. Fan, L. Tang, Y. Liu, Z. Gong, T. Wu, X. Zhen, C. Feng, H. Feng, L. Wang, L. Xu, M. Yan, Reveal Bronsted-Evans-Polanyi relation and attack mechanisms of reactive oxygen species for photocatalytic H₂O₂ production, *Appl. Catal. B* 301 (2022), 120757.
- [9] L. Zhou, J. Feng, B. Qiu, Y. Zhou, J. Lei, M. Xing, L. Wang, Y. Zhou, Y. Liu, J. Zhang, Ultrathin g-C₃N₄ nanosheet with hierarchical pores and desirable energy band for highly efficient H₂O₂ production, *Appl. Catal. B* 267 (2020), 118396.
- [10] Y. Yang, B. Zhu, L. Wang, B. Cheng, L. Zhang, J. Yu, In-situ grown N, S co-doped graphene on TiO₂ fiber for artificial photosynthesis of H₂O₂ and mechanism study, *Appl. Catal. B* 317 (2022), 121788.
- [11] Y. Zhao, X. Li, X. Fan, H. Wang, Y.L. Liu, Y. Chen, T. Yang, J. Ye, H. Huang, H. Li, X. Zhang, Y. Liu, H. Lin, Z. Kang, Small-molecule catalyzed H₂O₂ production via a phase-transfer photocatalytic process, *Appl. Catal. B* 314 (2022), 121499.
- [12] J. He, P. Lyu, B. Jiang, S. Chang, H. Du, J. Zhu, H. Li, A novel amorphous alloy photocatalyst (NiB/In₂O₃) composite for sunlight-induced CO₂ hydrogenation to HCOOH, *Appl. Catal. B* 298 (2021), 120603.
- [13] A. Li, Q. Cao, G. Zhou, B. Schmidt, W. Zhu, X. Yuan, H. Huo, J. Gong, M. Antonietti, Three-phase photocatalysis for the enhanced selectivity and activity of CO₂ reduction on a hydrophobic surface, *Angew. Chem. Int. Ed.* 58 (2019) 14549–14555.
- [14] L. Li, L. Xu, Z. Hu, J. Yu, Enhanced mass transfer of oxygen through a gas-liquid-solid interface for photocatalytic hydrogen peroxide production, *Adv. Funct. Mater.* 31 (2021) 2106120.
- [15] L. Chen, S. Li, Z. Yang, C. Chen, C. Chu, B. Chen, Enhanced photocatalytic hydrogen peroxide production at a solid-liquid-air interface via microenvironment engineering, *Appl. Catal. B* 305 (2022), 121066.
- [16] M. Sun, X. Wang, Y. Li, H. Pan, M. Murugananthan, Y. Han, J. Wu, M. Zhang, Y. Zhang, Z. Kang, Bifunctional Pd-O_x center at the liquid-solid-gas triphase interface for H₂O₂ photosynthesis, *ACS Catal.* 12 (2022) 2138–2149.
- [17] H. Huang, Q. Zhang, R. Shi, C. Su, Y. Wang, J. Zhao, T. Zhang, Synergistic effect of triphase interface and fluid control for efficient photosynthesis of residue-free H₂O₂, *Appl. Catal. B* 317 (2022), 121731.
- [18] B. He, Z. Wang, P. Xiao, T. Chen, J. Yu, L. Zhang, Cooperative coupling of H₂O₂ production and organic synthesis over a floatable polystyrene-sphere-supported TiO₂/Bi₂O₃ S-scheme photocatalyst, *Adv. Mater.* 34 (2022) 2203225.
- [19] R. He, D. Xu, X. Li, Floatable S-scheme photocatalyst for H₂O₂ production and organic synthesis, *J. Mater. Sci. Technol.* 138 (2023) 256–258.
- [20] Y. Fu, C. Liu, M. Zhang, C. Zhu, H. Li, H. Wang, Y. Song, H. Huang, Y. Liu, Z. Kang, Photocatalytic H₂O₂ and H₂ generation from living *Chlorella vulgaris* and carbon micro particle comodified g-C₃N₄, *Adv. Energy Mater.* 8 (2018) 1802525.
- [21] G. Han, F. Xu, B. Cheng, Y. Li, J. Yu, L. Zhang, Enhanced photocatalytic H₂O₂ production over inverse opal ZnO@polydopamine S-scheme heterojunctions, *Acta Phys. -Chim. Sin.* 38 (2022) 2112037.
- [22] M. Gu, D. Lee, J. Mun, D. Kim, H.I. Cho, B. Kim, W. Kim, G. Lee, B.S. Kim, H.I. Kim, Solar-to-hydrogen peroxide conversion of photocatalytic carbon dots with anthraquinone: unveiling the dual role of surface functionalities, *Appl. Catal. B* 312 (2022), 121379.
- [23] X. Zhang, P. Ma, C. Wang, L. Gan, X. Chen, P. Zhang, Y. Wang, H. Li, L. Wang, X. Zhou, K. Zheng, Unraveling the dual defect sites in graphite carbon nitride for ultra-high photocatalytic H₂O₂ evolution, *Energy Environ. Sci.* 15 (2022) 830–842.
- [24] J. Liu, G. Hodes, J. Yan, S. Liu, Metal-doped Mo₂C (metal = Fe, Co, Ni, Cu) as catalysts on TiO₂ for photocatalytic hydrogen evolution in neutral solution, *Chin. J. Catal.* 42 (2021) 205–216.
- [25] B. Zhu, B. Cheng, J. Fan, W. Ho, J. Yu, g-C₃N₄-based 2D/2D composite heterojunction photocatalyst, *Small Struct.* 2 (2021) 2100086.
- [26] Z. Mei, G. Wang, S. Yan, J. Wang, Rapid microwave-assisted synthesis of 2D/1D ZnIn₂S₄/TiO₂ S-scheme heterojunction for catalyzing photocatalytic hydrogen evolution, *Acta Phys. -Chim. Sin.* 37 (2021) 2009097.
- [27] L. Zhang, J. Zhang, H. Yu, J. Yu, Emerging S-scheme photocatalyst, *Adv. Mater.* 34 (2022) 2107668.
- [28] Z. Jiang, B. Cheng, Y. Zhang, S. Wageh, A.A. Al-Ghamdi, J. Yu, L. Wang, S-scheme ZnO/WO₃ heterojunction photocatalyst for efficient H₂O₂ production, *J. Mater. Sci. Technol.* 124 (2022) 193–201.
- [29] K. Li, S. Zhang, Y. Li, J. Fan, K. Lv, MXenes as noble-metal-alternative co-catalysts in photocatalysis, *Chin. J. Catal.* 42 (2021) 3–14.
- [30] C. Bie, H. Yu, B. Cheng, W. Ho, J. Fan, J. Yu, Design, fabrication, and mechanism of nitrogen-doped graphene-based photocatalyst, *Adv. Mater.* 33 (2021) 2003521.
- [31] M. Sayed, F. Xu, P. Kuang, J. Low, S. Wang, L. Zhang, J. Yu, Sustained CO₂-photoreduction activity and high selectivity over Mn, C-codoped ZnO core-triple shell hollow spheres, *Nat. Commun.* 12 (2021) 4936.
- [32] L. Qin, Y. Lin, Y. Dou, Y. Yang, K. Li, T. Li, F. Liu, Toward enhanced photocatalytic activity of graphite carbon nitride through rational design of noble metal-free dual cocatalysts, *Nanoscale* 12 (2020) 13829–13837.
- [33] D. Gao, J. Xu, L. Wang, B. Zhu, H. Yu, J. Yu, Optimizing atomic hydrogen desorption of sulfur-rich NiS_{1+x} cocatalyst for boosting photocatalytic H₂ evolution, *Adv. Mater.* 34 (2022) 2108475.
- [34] C. Bie, B. Zhu, L. Wang, H. Yu, C. Jiang, T. Chen, J. Yu, A bifunctional CdS/MoO₃/MoS₂ catalyst enhances photocatalytic H₂ evolution and pyruvic acid synthesis, *Angew. Chem. Int. Ed.* 61 (2022), e202212045.
- [35] R. Serra-Maia, S. Chastka, M. Bellier, T. Douglas, J.D. Rimstidt, F.M. Michel, Effect of particle size on catalytic decomposition of hydrogen peroxide by platinum nanocatalysts, *J. Catal.* 373 (2019) 58–66.
- [36] M.R. Horn, A. Singh, S. Alomari, S. Goberna-Ferrón, R. Benages-Vilau, N. Chodankar, N. Motta, K. Ostrikov, J. MacLeod, P. Sonar, P. Gomez-Romero, D. Dubal, Polyoxometalates (POMs): from electroactive clusters to energy materials, *Energy Environ. Sci.* 14 (2021) 1652–1700.
- [37] X. Meng, H. Wang, S. Song, H. Zhang, Proton-conducting crystalline porous materials, *Chem. Soc. Rev.* 46 (2017) 464–480.
- [38] Y. Liu, C. Tang, M. Cheng, M. Chen, S. Chen, L. Lei, Y. Chen, H. Yi, Y. Fu, L. Li, Polyoxometalate@metal-organic framework composites as effective photocatalysts, *ACS Catal.* 11 (2021) 13374–13396.
- [39] S.H. Park, J. Kim, W.E. Lee, D.J. Byun, M.H. Kim, One-step synthesis of hollow dimpled polystyrene microparticles by dispersion polymerization, *Langmuir* 33 (2017) 2275–2282.
- [40] Q. Yin, J. Tan, C. Besson, Y.V. Geletii, D.G. Musaev, A.E. Kuznetsov, Z. Luo, K. I. Hardcastle, C.L. Hill, A fast soluble carbon-free molecular water oxidation catalyst based on abundant metals, *Science* 328 (2010) 342–345.
- [41] B. Guan, L. Yu, J. Li, X. Lou, A universal cooperative assembly-directed method for coating of mesoporous TiO₂ nanoshells with enhanced lithium storage properties, *Sci. Adv.* 2 (2016), e1501554.
- [42] W. Sun, B. An, B. Qi, T. Liu, M. Jin, C. Duan, Dual-excitation polyoxometalate-based frameworks for one-pot light-driven hydrogen evolution and oxidative dehydrogenation, *ACS Appl. Mater. Interfaces* 10 (2018) 13462–13469.

- [43] Z. Jiang, Y. Zhang, L. Zhang, B. Cheng, L. Wang, Effect of calcination temperatures on photocatalytic H₂O₂-production activity of ZnO nanorods, *Chin. J. Catal.* 43 (2022) 226–233.
- [44] G.-h Moon, W. Kim, A.D. Bokare, N.-e Sung, W. Choi, Solar production of H₂O₂ on reduced graphene oxide–TiO₂ hybrid photocatalysts consisting of earth-abundant elements only, *Energy Environ. Sci.* 7 (2014) 4023–4028.
- [45] D. Tsukamoto, A. Shiro, Y. Shiraishi, Y. Sugano, S. Ichikawa, S. Tanaka, T. Hirai, Photocatalytic H₂O₂ production from ethanol/O₂ system using TiO₂ loaded with Au–Ag bimetallic alloy nanoparticles, *ACS Catal.* 2 (2012) 599–603.
- [46] W. Guo, H. Lv, Z. Chen, K.P. Sullivan, S.M. Lauinger, Y. Chi, J.M. Sumliner, T. Lian, C.L. Hill, Self-assembly of polyoxometalates, Pt nanoparticles and metal–organic frameworks into a hybrid material for synergistic hydrogen evolution, *J. Mater. Chem. A* 4 (2016) 5952–5957.
- [47] S. Wageh, Ahmed A. Al-Ghamdi, Omar A. Al-Hartomy, Maged F. Alotaibi, W. L. CdS/polymer S-scheme H₂-production photocatalyst and its in-situ irradiated electron transfer mechanism, *Chin. J. Catal.* 43 (2022) 586–588.
- [48] H. Li, B. Sun, T. Gao, H. Li, Y. Ren, G. Zhou, Ti₃C₂ MXene co-catalyst assembled with mesoporous TiO₂ for boosting photocatalytic activity of methyl orange degradation and hydrogen production, *Chin. J. Catal.* 43 (2022) 461–471.
- [49] P. Wang, H. Li, Y. Cao, H. Yu, Carboxyl-functionalized graphene for highly efficient H₂-evolution activity of TiO₂ photocatalyst, *Acta Phys. -Chim. Sin.* 37 (2021) 2008047.
- [50] Q. Liu, J. Huang, H. Tang, X. Yu, J. Shen, Construction 0D TiO₂ nanoparticles/2D CoP nanosheets heterojunctions for enhanced photocatalytic H₂ evolution activity, *J. Mater. Sci. Technol.* 56 (2020) 196–205.
- [51] Y. Yang, Z. Zeng, G. Zeng, D. Huang, R. Xiao, C. Zhang, C. Zhou, W. Xiong, W. Wang, M. Cheng, W. Xue, H. Guo, X. Tang, D. He, Ti₃C₂ MXene/porous g-C₃N₄ interfacial Schottky junction for boosting spatial charge separation in photocatalytic H₂O₂ production, *Appl. Catal. B* 258 (2019), 117956.
- [52] Y. Kofuji, S. Ohkita, Y. Shiraishi, H. Sakamoto, S. Tanaka, S. Ichikawa, T. Hirai, Graphitic carbon nitride doped with biphenyl diimide: efficient photocatalyst for hydrogen peroxide production from water and molecular oxygen by sunlight, *ACS Catal.* 6 (2016) 7021–7029.
- [53] S. Wageh, Ahmed A. Al-Ghamdi, Q. Xu, Core-shell Au@NiS_{1+x} cocatalyst for excellent TiO₂ photocatalytic H₂ production, *Acta Phys. -Chim. Sin.* 38 (2022) 2202001.
- [54] B. He, C. Bie, X. Fei, B. Cheng, J. Yu, W. Ho, A.A. Al-Ghamdi, S. Wageh, Enhancement in the photocatalytic H₂ production activity of CdS NRs by Ag₂S and NiS dual cocatalysts, *Appl. Catal. B* 288 (2021), 119994.
- [55] S. Mukhopadhyay, J. Debgupta, C. Singh, A. Kar, S.K. Das, A kegginn polyoxometalate shows water oxidation activity at neutral pH: POM@ZIF-8, an efficient and robust electrocatalyst, *Angew. Chem. Int. Ed.* 57 (2018) 1918–1923.